Displacive Phase Transitions in and Strain Analysis of Fe-Doped CaTiO₃ Perovskites at High Temperatures by Neutron Diffraction

A. I. Becerro,*,[1] S. A. T. Redfern,† M. A. Carpenter,† K. S. Knight,‡ and F. Seifert*

*Bayerisches Geoinstitut, Universität Bayreuth, 95440-Bayreuth, Germany; †Department of Earth Sciences, University of Cambridge, Cambridge CB2 3EQ, United Kingdom; and ‡Rutherford Appleton Laboratory, Chilton, Didcot OX11 0QX, United Kingdom

The influence of small amounts of Fe^{3+} on the phase transitions of $CaTiO_3$ perovskite has been studied by means of in situ high-temperature neutron diffraction. The same sequence of phase transitions as observed in $CaTiO_3$ is shown by both $CaTi_{0.9}Fe_{0.1}O_{2.95}$ and $CaTi_{0.8}Fe_{0.2}O_{2.90}$ perovskites: from orthorhombic *Pnma* symmetry at room temperature (RT) to cubic $Pm\bar{3}m$ at high temperature, with an intermediate $I4/mcm$ tetragonal phase which exists over a temperature range of about 100°C. The two phase boundaries in the temperature vs composition phase diagram of the system $CaFe_xTi_{1-x}O_{3-x/2}$ ($0 \leq x \leq 0.4$) decrease in a quasi-linear manner with increasing Fe content up to $x = 0.2$ and then they both drop abruptly to RT. The existence of a second orthorhombic phase (*Cmcm*), which has been postulated for $CaTiO_3$, is ruled out in the Fe-doped $CaTiO_3$ perovskites in view of the behavior of specific diffraction peaks. Strain analysis shows first-order thermodynamic character for the $Pnma \rightarrow I4/mcm$ transition, while the character of the $Pm\bar{3}m \rightarrow I4/mcm$ transition could be second order or tricritical. Shear strains behave more or less classically, as described by order parameter coupling and shear strain/order parameter coupling models. The volume strain has an anomalous coupling with the order parameter components, which appears to be temperature-dependent. © 2002 Elsevier Science (USA)

Key Words: Perovskites; Fe-doped CaTiO₃; Phase transitions; Spontaneous strain; High-temperature neutron diffraction; *Cmcm*.

1. INTRODUCTION

Perovskite-type oxides of general formula ABO_3 (1) are important in material sciences, physics and earth sciences, e.g., for their electric properties and as the dominant mineral in the Earth's lower mantle. They are also well known for their phase transitions, which may strongly affect their physical and chemical properties. In the lower mantle, silicate perovskites are the dominant minerals, with $MgSiO_3$ as the main component. Recent experimental investigations (2) have shown that the phase transitions and properties of silicate perovskites are strongly influenced by the incorporation of minor elements such as Al or Fe. Detail investigations on silicate perovskites are difficult because of the extreme conditions of their synthesis (above 23 GPa for $MgSiO_3$), the small amount of sample available, the limitations of a precise control of oxygen fugacity, the instability of these phases in ex situ investigations, etc. In order to overcome these difficulties, we have chosen a more tractable model system, the solid solution $CaFe_xTi_{1-x}O_{3-x/2}$, as a convenient starting point to obtain basic knowledge of the influence of Fe on phase transitions and related aspects of $CaTiO_3$ perovskite.

Perovskites belonging to the system $CaFe_xTi_{1-x}O_{3-x/2}$ ($0 \leq x \leq 1$) exhibit a quasi-continuous variation of oxygen defect concentrations, from zero in $CaTiO_3$, to 0.5 per formula unit in $CaFeO_{2.5}$ (3). The $CaFeO_{2.5}$ end-member has a brownmillerite-type structure with alternating layers of octahedra and tetrahedra (4), the latter due to the clustering of oxygen vacancies into defect chains. Structures with fully ordered vacancies have also been described for $x = 0.67$ (5) and 0.5 (6), while partially ordered structures occur at lower Fe contents. The degree of ordering depends on the annealing temperature and vacancy concentration (7). However, when the Fe content is in the range $0 < x < 0.4$ and the samples are annealed at high temperatures, the oxygen vacancies are randomly distributed in the crystal which maintains the perovskite structure (8). A number of papers have been published describing the detailed mechanism and type of oxygen vacancy ordering in this system from both short- and long-range order points of view (7, 9).

In this paper we concentrate on low Fe content members of the system $CaFe_xTi_{1-x}O_{3-x/2}$ annealed at temperatures

---

such that the oxygen vacancies are randomly distributed in the crystal. The $CaTiO_3$ end-member is orthorhombic at room temperature (10) and transforms to the cubic ideal perovskite structure at high temperatures, with an intermediate tetragonal phase (11). The existence of a second orthorhombic phase before the transformation to tetragonal symmetry has been proposed (12) but is still unclear (13). On the other hand, phase transitions from orthorhombic to tetragonal and cubic symmetry have been reported with increasing Fe content at room temperature in the system $CaFe_xTi_{1-x}O_{3-x/2}$ for $0 \leq x \leq 0.4$. Thus, for $x \leq 0.205(17)$ the structures are orthorhombic and for $x \geq 0.251(29)$ they are cubic, the intermediate compositions showing tetragonal symmetry (8). The same sequence of phase transitions found in $CaTiO_3$ with increasing temperature is expected when small amounts of Ti^{4+} are replaced by Fe^{3+} in the perovskite structure, so that the orthorhombic and tetragonal phases found at RT would be the result of such phase transitions.

The objective of this study is to investigate the influence of small amounts of Fe^{3+} on the phase transitions of $CaTiO_3$ perovskite with increasing temperature by using the high-resolution powder diffractometer, HRPD, on the neutron spallation source at the Rutherford Appleton Laboratory. The high resolution of the diffractometer and the stability of the sample heater have permitted a rather precise characterization of the sequence of phase transitions undergone by two $CaFe_xTi_{1-x}O_{3-x/2}$ perovskite compounds ($x = 0.10$ and 0.20) heated to high temperatures. A phase diagram of the system $CaFe_xTi_{1-x}O_{3-x/2}$ ($0 \leq x \leq 0.4$) has been derived and spontaneous strains analysis has provided an indication of how the driving order parameters for the transitions actually evolve.

2. EXPERIMENTAL

Two powder samples of $CaFe_xTi_{1-x}O_{3-x/2}$, with nominal compositions $x = 0.10$ and 0.20, were synthesized from mixtures of $CaCO_3$, TiO_2 and Fe_2O_3, by slow decarbonation and sintering at $1350°C$ with repeated intermittent grinding. These materials were then annealed in open Pt-capsules at $1200°C$ for 6 days in CO–CO_2 gas mixtures corresponding to oxygen fugacities one log unit above the iron–wustite equilibrium. Under these conditions all the iron in the samples is present as Fe^{3+}, the oxygen vacancies are randomly distributed in the crystal lattice (9a) and cubic symmetry is obtained. Samples were then drop quenched and examined ex situ by electron microprobe analysis. Chemical compositions have been calculated on the basis of two cations per formula unit and are $x = 0.0999(92)$ and $0.1886(97)$. The powders were further annealed as pressed pellets for a second period of 6 h at the same temperature and gas mixing conditions and they were then drop quenched.

Neutron powder diffraction patterns were collected with increasing temperature at the high-resolution powder diffractometer HRPD (14) at the ISIS spallation source. Approximately $2.5 \, cm^3$ of powder pressed as sintered pellets were contained in a thin-walled vanadium sample can with an internal diameter of $11 \, mm$. The can was connected to the center stick of a standard ISIS furnace (max. temperature $= 1100°C$) and the whole furnace was evacuated to $5 \times 10^{-4} \, mbar$. The sample temperature was measured using a chromel/alumel thermocouple mounted on the surface of the can approximately $2 \, cm$ from the neutron beam. During all runs the temperature variations were less than $\pm 2 \, K$. Data were collected in time-of-flight (TOF) mode using logarithmic time-channel binning of $\Delta t/t = 1 \times 10^{-4}$, from 30 to 130 ms, which corresponds to a measured d-spacing range of 0.60–$2.6 \, \text{Å}$ for the back-scattering detectors. The raw data from the detector banks were focused to a common scattering angle of $163.329°$, normalized to an upstream monitor and corrected for detector efficiency using a vanadium standard. Finally, the data were rebinned in the TOF range 32–$120 \, ms$, which gave the required resolution to detect the transition-related strains in the sample.

All the diffraction patterns were analyzed using the Rietveld method with the GSAS software (15). Refined parameters were background coefficients, lattice constants, linewidths, atomic positions and temperature factors.

3. RESULTS AND DISCUSSION

3.1. Phase Transitions and Phase Diagram

3.1.1. Phase Transitions

Figure 1 shows a restricted TOF region of selected normalized diffraction patterns of the $x = 0.20$ sample at three different temperatures. The presence of superlattice reflections in the low- and medium-temperature patterns can be seen in comparison with the pattern obtained at a high temperature (top of the figure). Superlattice reflections in perovskites can result from the correlated tilting of neighboring BO_6 octahedra and they can be used to identify the space group of the phase (16). The pattern recorded at $25°C$ (bottom pattern in Fig. 1) shows all the superlattice reflections characteristic of the orthorhombic $Pnma$ space group. In Glazer's notation (16) this space group corresponds to the tilt system $a^+b^-b^-$, i.e., an in-phase tilt about the tetrad axis ($[100]_{cubic}$ direction) and two equal out-of-phase tilts about the tetrad axis ($[010]$ and $[001]$ cubic directions). With increasing temperature, the $\{022,220\}_{Pnma}$, $\{112,031,211\}_{Pnma}$ and $\{102,201\}_{Pnma}$ set of reflections progressively converge, so that at $T = 820°C$ (middle pattern in Fig. 1) the two former sets form single peaks and the latter disappears. The superlattice reflections of this pattern are indicative of tetragonal symmetry and
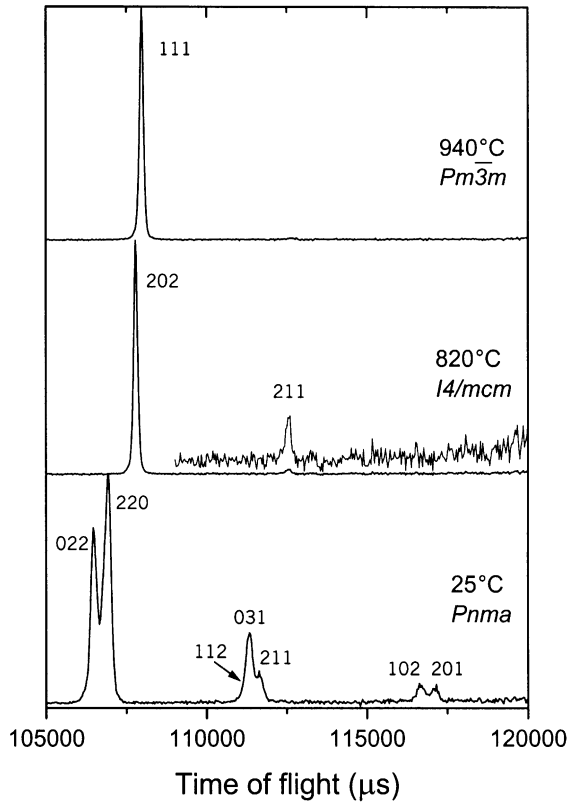
FIG. 1. Selected TOF region of three normalized diffraction patterns of $CaFe_{0.20}Ti_{0.80}O_{2.90}$ at three different temperatures. Note the systematic disappearance of the superlattice reflections when the temperature increases. Multiplication factor of middle plot = 10.

space group $I4/mcm$. The tilt system corresponding to this space group is $a^0a^0c^-$, where two of the tilts are removed with respect to the $Pnma$ tilt system and there is one single out-of-phase tilt about the tetrad axis. With increasing temperature from 820°C, the intensity of the superlattice reflection $211_{I4/mcm}$ systematically decreases and at 940°C it completely disappears (top pattern in Fig. 1). At $T \geq 940$°C the diffraction patterns do not show evidence of any superlattice reflections and they are compatible with the cubic space group $Pm\bar{3}m$ ($a^0a^0a^0$).

The same behavior of superlattice reflections is observed when heating the $x = 0.10$ sample, with a transition temperature for the orthorhombic $Pnma \rightarrow$ tetragonal $I4/mcm$ transition of ~ 1030°C. The maximum temperature of the furnace (1100°C) was not sufficient to transform this perovskite to the cubic structure.

The diffraction patterns recorded at increasing temperatures for both perovskites were then indexed in the appropriate space groups and the cell parameters refined by means of the Rietveld method using GSAS software (15). Structural parameters and reliability factors obtained from typical Rietveld refinements for every space group of

TABLE 1
Representative Structural Parameters for the Phases of $CaTi_{0.9}Fe_{0.1}O_{2.95}$

Atom	Site	x	y	z	B (Å²)
Pnma 300°C, $a=$ 5.4461(1) Å, $b=$ 7.6786(1) Å, $c=$ 5.4151(1)Å					
Ca	4c	0.0257(3)	0.25	−0.0055(4)	1.46(3)
Ti,Fe	4b	0.5	0	0	0.79(3)
O1	4c	0.4867(3)	0.25	0.0679(3)	1.27(2)
O2	8d	0.2877(2)	0.0341(1)	0.7124(2)	1.32(2)
I4/mcm 1100°C, $a=$ 5.4927(1) Å, $b=$ 5.4927(1) Å, $c=$ 7.7703(2) Å					
Ca	4b	0	0.5	0.25	3.24(2)
Ti,Fe	4c	0	0	0	0.79(1)
O1	4a	0	0	0.25	3.81(3)
O2	8h	0.2664(4)	0.7664(4)	0	5.85(3)

Note. The standard R factors (in %) for both structural refinements are: 300°C *Pnma*: $wR_p = 4.79$, $R_p = 4.31$, $\chi^2 = 4.08$; 1100°C *I4/mcm*: $wR_p = 6.78$, $R_p = 4.97$, $\chi^2 = 5.2$. The numbers in parentheses indicate standard deviations, in units of the least-significant figures, as estimated in the GSAS computer program.

the $x = 0.10$ and 0.20 samples are given in Tables 1 and 2, respectively. Figs. 2a and 2b show the observed, calculated and difference powder neutron diffraction patterns, corresponding to the refinements of Tables 1 and 2, respectively. Lattice parameters (in terms of the pseudocubic sub-cell) are plotted vs temperature in Figs. 3a and 3b for both samples. At both compositions, the orthorhombic cell edge

TABLE 2
Representative Structural Parameters for the Phases of $CaTi_{0.8}Fe_{0.2}O_{2.90}$

Atom	Site	x	y	z	B (Å²)
Pnma 25°C, $a=$ 5.4359(1) Å, $b=$ 7.6623(2) Å, $c=$ 5.4037(1) Å					
Ca	4c	0.02242(5)	0.25	−0.0051(6)	0.52(3)
Ti,Fe	4b	0.5	0	0	0.62(3)
O1	4c	0.4860(5)	0.25	0.0673(5)	1.15(2)
O2	8d	0.2866(3)	0.0352(3)	0.7144(4)	1.61(4)
I4/mcm 820°C, $a = b =$ 5.4726(1) Å, $c=$ 7.7412(4) Å					
Ca	4b	0	0.5	0.25	1.86(2)
Ti,Fe	4c	0	0	0	1.72(2)
O1	4a	0	0	0.25	7.5(5)
O2	8h	0.2664(4)	0.7664(4)	0	4.53(3)
Pm3m 940°C, $a = b = c =$ 3.8767(1) Å					
Ca	1b	0.5	0.5	0.5	2.08(1)
Ti,Fe	1a	0	0	0	1.09(1)
O	3d	0.5	0	0	5.69(3)

Note. The standard R factors (in %) for the three structural refinements are: 25°C *Pnma*: $wR_p = 8.00$, $R_p = 7.11$, $\chi^2 = 2.20$; 820°C *I4/mcm*: $wR_p = 8.67$, $R_p = 7.25$, $\chi^2 = 1.66$; 940°C *Pm3m*: $wR_p = 6.55$, $R_p = 5.13$, $\chi^2 = 2.54$. The numbers in parentheses indicate standard deviations, in units of the least significant figures, as estimated in the GSAS computer program.
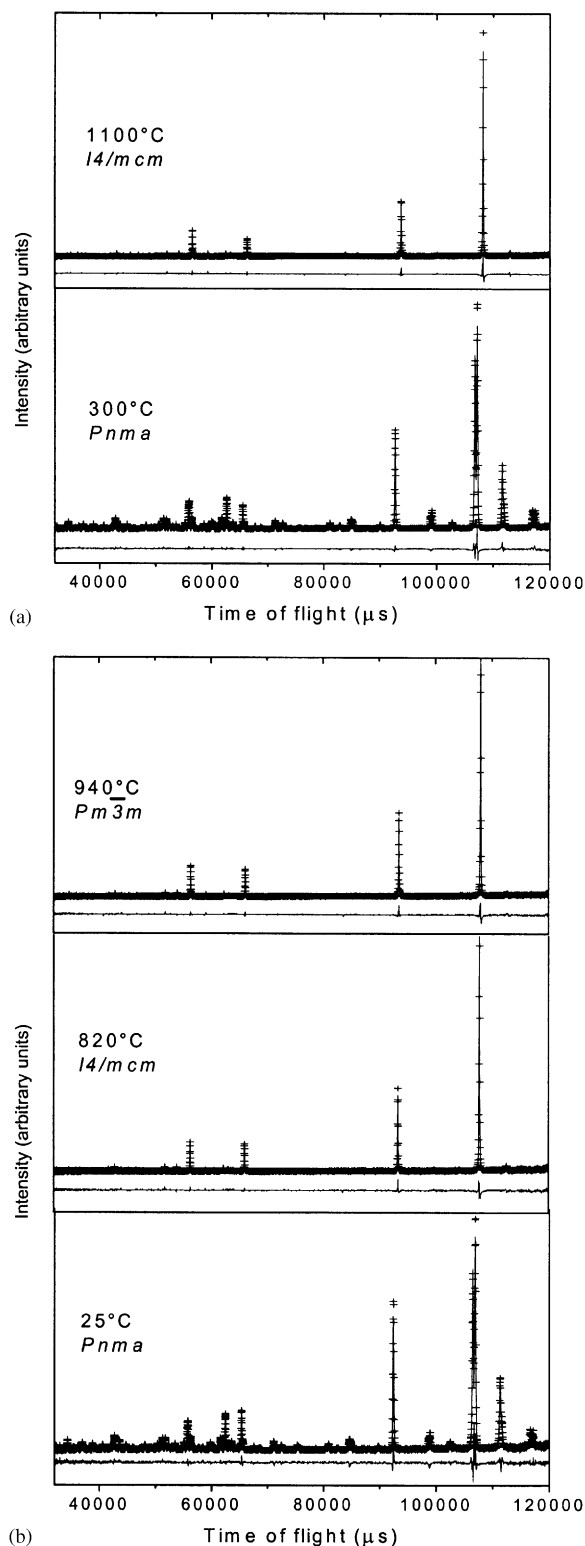
FIG. 2. Observed (+), calculated (—) and difference neutron powder diffraction patterns of $CaFe_{0.10}Ti_{0.90}O_{2.95}$ (a) and $CaFe_{0.20}Ti_{0.80}O_{2.90}$ (b) at representative temperatures corresponding to the characteristic space groups of the structure. Fig. 2a does not show the refinement corresponding to the $Pm\bar{3}m$ space group because the maximum temperature of the furnace was not sufficient to transform the $CaFe_{0.10}Ti_{0.90}O_{2.95}$ perovskite compound to the cubic symmetry. The structural parameters corresponding to these refinements are given in Tables 1 and 2, respectively.
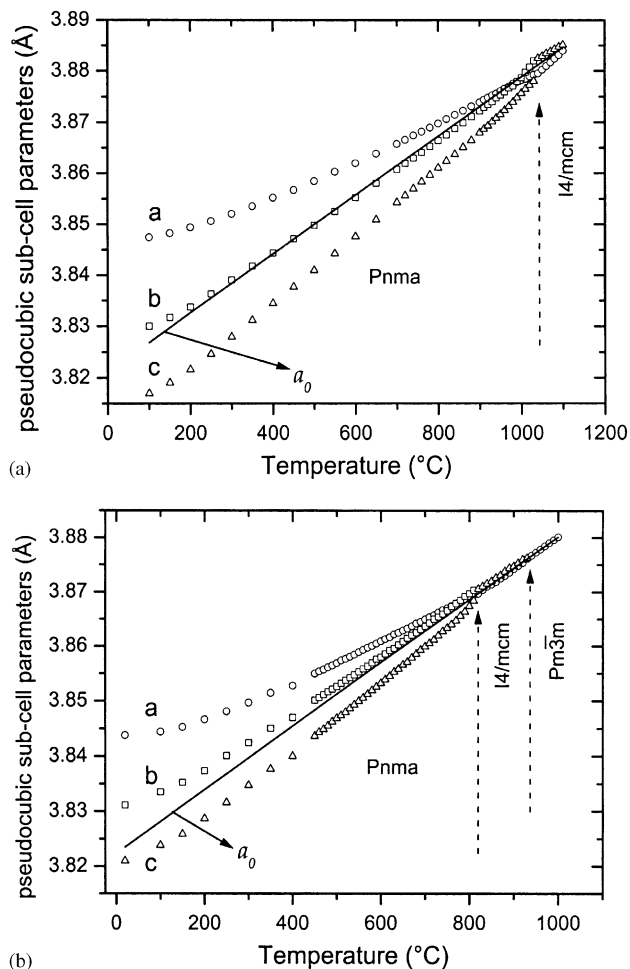

FIG. 3. Pseudocubic sub-cell parameters ($a = a_{cell}/\sqrt{2}$, $b = b_{cell}/\sqrt{2}$, $c = c_{cell}/2$, where a_{cell}, b_{cell} and c_{cell} are the lattice parameters of the orthorhombic or tetragonal cell) as a function of temperature for $CaFe_{0.10}Ti_{0.90}O_{2.95}$ (a) and $CaFe_{0.20}Ti_{0.80}O_{2.90}$ (b). The a_0 line is the extrapolation to room temperature of the behavior of the cubic structure. See text for this line in each composition. Transition temperatures are marked by arrows. The maximum temperature of the furnace available did not allow the transformation to cubic symmetry in the $x = 0.10$ sample.

lengths increase anisotropically in a non-linear manner with increasing temperature, the non-linearity being stronger at low temperatures and particularly pronounced in the a-direction. In pure $CaTiO_3$ perovskite this effect is much smaller and the behavior of the lattice parameters with temperature is described as "quasi-linear" and "nearly linear" by Redfern (11) and Kennedy *et al.* (12b), respectively.

An upper limit for the $I4/mcm \rightarrow Pm\bar{3}m$ transition temperature in the $CaTi_{0.9}Fe_{0.1}O_{2.95}$ perovskite has been estimated by linear extrapolation of the a and c tetragonal lattice parameters. They intersect at $\sim 1145°C$, and it can be assumed that the symmetry changes to cubic somewhere in the temperature interval $1100–1145°C$. Therefore, the sequence of space groups and transition temperatures

(in °C) for each of the Fe-containing CaTiO$_3$ perovskites is

$x = 0.10$:   1030(10)   1120(25)
$Pnma$ $\rightarrow$ $I4/mcm$ $\rightarrow$ $Pm\bar{3}m$.
$x = 0.20$:   815(5)   935(5)

Finally, Fig. 4 shows the behavior of the pseudocubic sub-cell volume with temperature for both iron-containing CaTiO$_3$ perovskites. The pseudocubic sub-cell volume of pure CaTiO$_3$—calculated from data in Refs. (11, 12b)—has also been plotted for comparison. The following comments can be made from the evolution of the cell volume in the three samples: (i) In the Fe-containing perovskites volumes increase without break or discontinuity with increasing temperature. Pure CaTiO$_3$ shows, apparently, the same behavior; however, Kennedy et al. (12b) pointed out the presence of a discontinuity close to 1100°C which we cannot really see by plotting their data. (ii) In detail, the volume vs temperature curves in Fig. 4 show a change in slope at the temperature of the $Pnma$–$I4/mcm$ phase transition, with the high-temperature phase having a lower thermal expansivity than the low-temperature phase. (iii) There is a clear relationship between the cell volume and the Fe content of the samples, so that the higher the Fe content, the higher the volume. The reason for this is the larger ionic radius of Fe^{3+} compared to Ti^{4+} for any of the coordination numbers expected in these structures (9a).

3.1.2. Is There an Intermediate Orthorhombic Phase?

The sequence of space groups found here for both Fe-bearing perovskites is the same as that reported by Redfern (11) for CaTiO$_3$. However, Guyot et al. (12a) have found
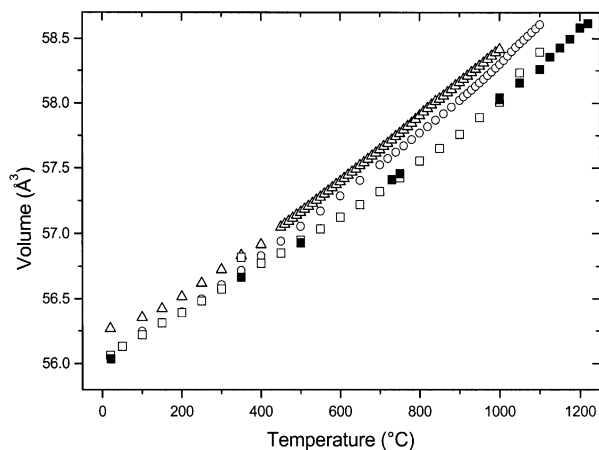

FIG. 4. Pseudocubic sub-cell volume as a function of temperature for CaFe$_{0.10}$Ti$_{0.90}$O$_{2.95}$ (circles), CaFe$_{0.20}$Ti$_{0.80}$O$_{2.90}$ (triangles) and CaTiO$_3$ (open squares: data from Redfern (11) and solid squares: data from Kennedy et al. (12b)).

two specific heat anomalies in CaTiO$_3$, the low-temperature anomaly being assigned to an orthorhombic $Pnma$–orthorhombic $Cmcm$ transition and the high-temperature anomaly to a combination of $Cmcm$–$I4/mcm$ and $I4/mcm$–$Pm\bar{3}m$ transitions. Kennedy et al. (12b) were not able to distinguish between the two orthorhombic space groups because the qualities of the fits obtained by Rietveld analysis were comparable. The only weak evidence that they found for the existence of a second orthorhombic phase was a small discontinuity in the temperature dependence of the cell volume and octahedral tilt angles that coincides with the temperature reported by Guyot et al. (12a) for the $Pnma$–$Cmcm$ transition. A strain analysis of the CaTiO$_3$ unit cell by Carpenter et al. (13), using the parameters reported by Kennedy et al. (12b) for both orthorhombic phases, demonstrated that the evidence for an intermediate $Cmcm$ structure on heating CaTiO$_3$ remains ambiguous.

The $Pnma$ and $Cmcm$ structures are very closely related in perovskite-type oxides. The transition from $Pnma$ space group ($a^+b^-b^-$) to $Cmcm$ ($a^0b^+c^-$) involves the disappearance of one of the two octahedral rotations and the doubling of the unit cell volume with the c-axis being unchanged. The transition is required by symmetry to be of first order and, therefore, discontinuous. The diffraction patterns of both phases are very similar, and only differ in the splitting of some reflections in $Pnma$ and in the presence of very weak superlattice peaks in $Cmcm$.

The first evidence for the non-existence of a $Cmcm$ phase when heating CaFe$_{0.10}$Ti$_{0.90}$O$_{2.95}$ and CaFe$_{0.20}$Ti$_{0.80}$O$_{2.90}$ perovskites could be the absence of any discontinuity in the evolution of the unit cell volume in the temperature range where the transition is expected, as shown in Fig. 4. However, this behavior could be due to the tilt angles (or displacements of the oxygen atoms) being too small to produce appreciable changes in the unit cell volume. This is the case of CaGeO$_3$ where a $Pnma$ to $Cmcm$ transition seems to occur with no discontinuity in the unit cell volume (17). In fact, the $Pnma \rightarrow I4/mcm$ transition in our Fe-doped CaTiO$_3$ perovskites is also required by symmetry to be of first order. However, only a discrete change of slope but no discontinuity is observed in the volume for either of the samples, probably due to the same argument.

A more definitive conclusion related to the presence or absence of a $Cmcm$ phase on heating the Fe-bearing perovskites can be drawn from the splitting of peaks that differentiates between the orthorhombic space groups. As pointed out above, some lines that are split in $Pnma$ become a singlet in $Cmcm$. This is the case for the $\{022,220\}_{Pnma}$ reflections, which form a single 222 reflection in $Cmcm$. Fig. 5 shows the TOF region of diffraction patterns of the $x = 0.20$ sample, where these reflections occur. We only show patterns recorded at $T \leq 810$°C because, at temperatures above this, the orthorhombic
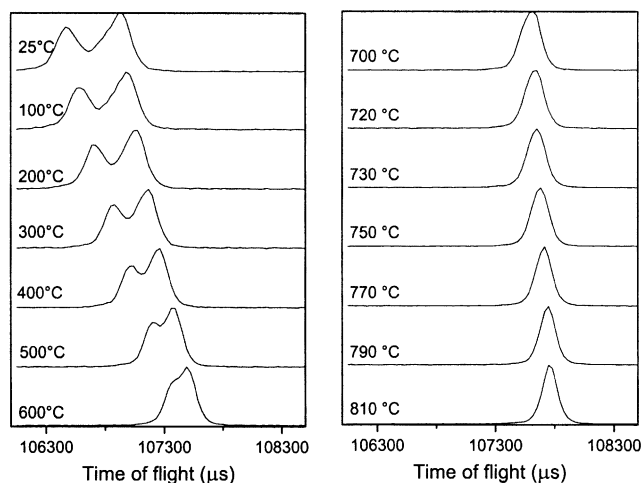
FIG. 5. TOF region of diffraction patterns of $CaFe_{0.20}Ti_{0.80}O_{2.90}$ where the $\{022,220\}_{Pnma}$ reflections and $\{222\}_{Cmcm}$ reflections are expected. The patterns correspond to temperatures just below the transition to tetragonal symmetry.

reflections disappear and the symmetry changes to tetragonal. The splitting of the lines is clear up to a temperature of 700°C, where the diffraction peak seems to contain only a single line. If this were the case, *Cmcm* would have a stability field from 700°C to 810°C, where a *Cmcm*–*I4/mcm* transition would occur. However, if the full-width at half-height (FWHH) of the peak is plotted vs temperature (Fig. 6a), a continuous linear decrease is observed up to the temperature at which the transition to tetragonal symmetry takes place (815(5)°C). At temperatures ≥820°C, where the material shows first tetragonal and then cubic symmetry, the FWHH is constant as expected from the single nature of the corresponding reflections (202 in *I4/mcm* and 111 in *Pm$\bar{3}$m*). Therefore, the $\{022,220\}_{Pnma}$ reflections converge continuously with increasing temperature and form a single line at the same temperature as the orthorhombic reflections disappear. This indicates that *Pnma* is the only orthorhombic space group of the structure present until the transformation to tetragonal symmetry. The same behaviour is observed in the patterns of the $x = 0.10$ sample (Fig. 6b), thus confirming the absence of a *Cmcm* structure in either of the Fe-doped CaTiO$_3$ perovskites. Two studies have been recently published which show that the *Cmcm* structure does not exist either in Sr-doped CaTiO$_3$ perovskites (18).

3.1.3. Phase Diagram

Based on the transition temperatures given above for the $CaFe_{0.10}Ti_{0.90}O_{2.95}$ and $CaFe_{0.20}Ti_{0.80}O_{2.90}$ perovskites, and using the transition temperature data for CaTiO$_3$ given by Kennedy *et al.* (12b) a quasi-linear and parallel decrease in phase boundaries is observed in the composi-
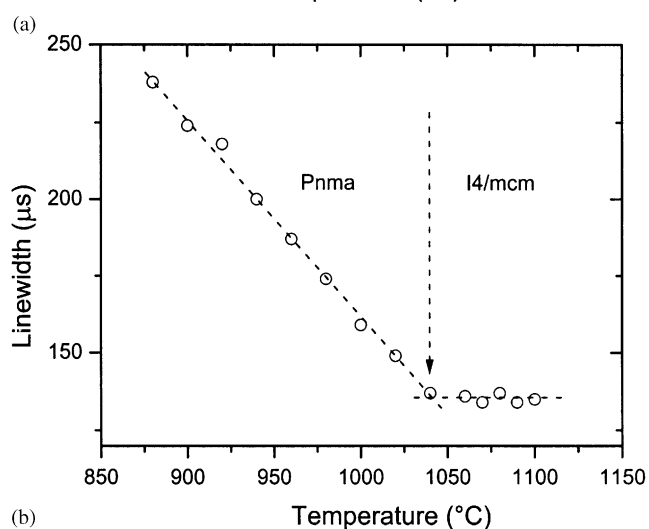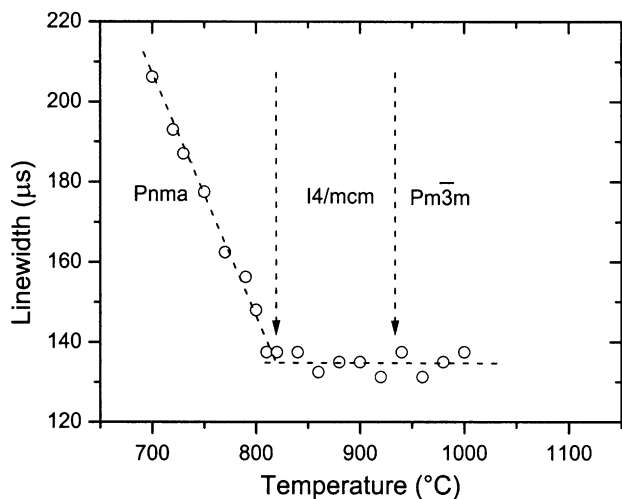

FIG. 6. Full-width at half-height (FWHH) of the peak in the TOF region shown in Fig. 5, where the $\{022,220\}_{Pnma}$ and $\{222\}_{Cmcm}$ reflections are expected: (a) for the $CaFe_{0.20}Ti_{0.80}O_{2.90}$ sample and (b) for the $CaFe_{0.10}Ti_{0.90}O_{2.95}$ sample. The presence of two converging lines all the way through the orthorhombic field can be easily inferred in both samples, demonstrating the non-existence of a *Cmcm* space group in either of the Fe-doped perovskites. The dotted lines are guides to the eye.

tional range $0 \le x \le 0.20$ of the temperature vs composition phase diagram (Fig. 7).

In a previous X-ray diffraction study (8), we obtained the following space groups and transition compositions at RT for samples quenched from the disordered-cubic field:

$$Pnma \stackrel{x=0.205\pm0.017}{\rightarrow} I4/mcm \stackrel{x=0.251\pm0.029}{\rightarrow} Pm\bar{3}m.$$
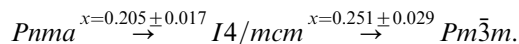
If the nature of the displacive phase transitions obtained by quenching (Ref. (8)) and by in situ heating up the samples (this study) is the same, this would imply that both phase boundaries drop drastically to RT near $x \sim 0.20-0.25$ (Fig. 7).
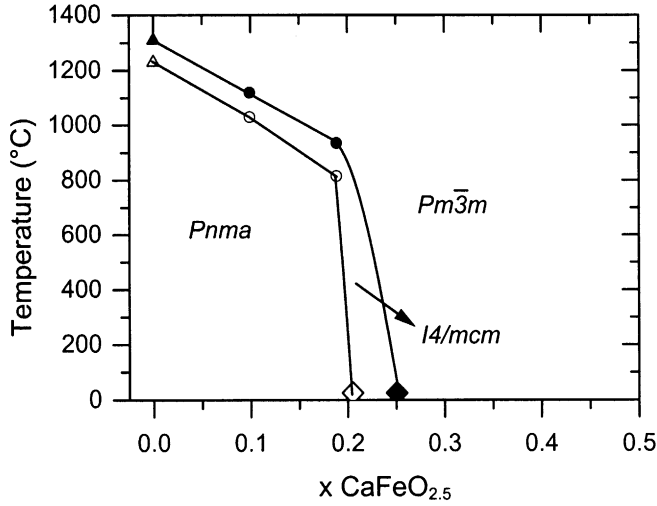
FIG. 7. Phase diagram as a function of temperature and composition showing the displacive phase transitions that take place on the system CaTiO$_3$–CaFeO$_{2.5}$: $Pnma \rightarrow I4/mcm$ (open symbols) and $I4/mcm \rightarrow Pm\bar{3}m$ (solid symbols). Triangles: Data from Kennedy *et al.* (12b). Circles: this study. Diamonds: Becerro *et al.* (8). The size of the error bars is $\sim$ the symbol size.

The transitions from $Pnma$ to $I4/mcm$ to $Pm\bar{3}m$ can be modeled in terms of a Landau free energy in which the chemical composition of the sample couples to the order parameters for the transition. For example, if we consider only the $I4/mcm - Pm\bar{3}m$ transition initially, a general Landau expansion for the excess free energy of the transition can be written as

$$\Delta G(Q) = \frac{a}{2}(T - T_c)Q^2 + \frac{b}{4}Q^4 + \frac{c}{6}Q^6 + \sum_i \lambda_i e_i Q^2$$
$$+ \frac{1}{2}\sum_{ik} C_{ik}^0 e_i e_k + \xi_1 X Q^2 + \xi_2 X Q^4,$$

where λ_i are the coupling coefficients between the spontaneous strains, e_i, and the order parameter, Q, and C_{ik}^0 are bare elastic moduli (excluding the influence of the phase transition). Here, the solute defect content, X, couples with the order parameter in the form $\xi_1 X Q^2 + \xi_2 X Q^4$. If it is assumed that the transition is tricritical in character at some composition X_{tri} (both Carpenter *et al.* (13) and Street (19) have suggested that the transition from $I4/mcm$ to $Pm\bar{3}m$ can be tricritical in pure CaTiO$_3$), then the expansion can be rewritten as

$$\Delta G(Q) = \frac{a}{2}(T - T_c)Q^2 + \xi(X - X_{tri})Q^4 + \frac{c}{6}Q^6$$
$$+ \sum_i \lambda_i e_i Q^2 + \frac{1}{2}\sum_{ik} C_{ik} e_i e_k + \xi' X Q^2,$$

where ξ' is a constant. If the solute defect concentration couples with the order parameter in this form, then the variation of T_c with composition need not be linear.

Indeed, a term of the form $\xi'' X^2 Q^2$, giving biquadratic coupling between Q and X, would give a parabolic $T-X$ relationship which approximates the behavior of the phase boundary between $I4/mcm$ and $Pm\bar{3}m$ fields in Fig. 7. Similar models can be constructed to explain the parallel nature of the phase boundary between $Pnma$ and $I4/mcm$. In each case, the influence of varying composition, X, is to modify the relative sizes of the effective prefactors of Q^n in the Landau expansion, and to modify the transition temperature in $T-X$ space along the lines shown in Fig. 7.

This model, however, describes a linear or a parabolic behavior of the phase boundaries in the T vs X diagram but not the very pronounced kink at $x = 0.20$ which is observed. It is then necessary to consider the possible differences in the nature of the displacive phase transitions that take place on quenching and on heating in Fe-rich structures. At this point we need to look at the regions of ordered and disordered structures in the phase diagram (7) reproduced here as Fig. 8. Partially and fully ordered structures appear as a consequence of the clustering of oxygen vacancies. The two displacive phase transitions observed on heating up the $x = 0.1$ sample occur at 1030°C and 1120°C, as this study shows. The phase diagram of Fig. 8 shows that, for this composition, the order–disorder phase transition takes place at a temperature slightly below 900°C. Based on previous studies (9c), no significant ordering of oxygen vacancies is expected during heating up on the time scale of the neutron measurement. Therefore, what we observe in the $x = 0.10$ sample are displacive phase transitions under stable equilibrium conditions. For the $x = 0.20$ composition, the order–disorder transition
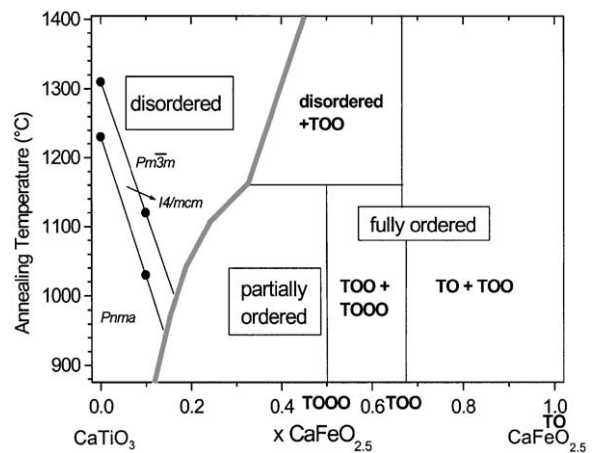

FIG. 8. Regions of disordered, partially ordered and fully ordered structures in the system CaTiO$_3$–CaFeO$_{2.5}$. (Taken from Ref. (7)). Symbols TO, TOO and TOOO indicate the sequence of tetrahedral (T) and octahedral (O) layers in the ordered structures. Displacive phase transitions shown in Fig. 7 have been incorporated here.

takes place at ca. 1050°C while the displacive phase transitions are at 815°C and 935°C and are, actually, in the metastable state (the more stable state would be the partially ordered structure according to the phase diagram of Fig. 8). For any composition more iron rich than $x = 0.20$ the stability field of the partially ordered field extends to higher temperatures where the rate of ordering will be much faster. This means that crystals with more Fe rich compositions than $x = 0.20$ might experience some ordering even during the short time scale of the quenching process. Actually, such an example of ordering during quenching has been shown for a composition $x = 0.38$ annealed in the region of the disordered structures (see Fig. 5b in Ref. (9a)). The displacive phase transitions appear to be suppressed by the ordering, giving the apparently abrupt change in transition temperatures as a function of composition.

In conclusion we can say that the boundaries of the orthorhombic $Pnma$, tetragonal $I4/mcm$ and cubic $Pm\bar{3}m$ fields in the T vs X phase diagram of the system $CaTiO_3$–$CaFeO_{2.5}$ decrease in a quasi-linear manner with increasing Fe content up to $x = 0.20$ and that, above that composition, the ordering of oxygen vacancies interferes with the displacive phase transitions which would take place in the region of the partially ordered structures.

3.2. Strain Analysis of the Transitions

3.2.1. Landau Theory: Symmetry-Adapted Strains and Their Coupling with the Order Parameter Components

Carpenter *et al.* (13) presented a single Landau free energy expansion (Eq. [1] in that paper) which contains six-order parameter components ($q_1 - q_6$) for the description of phase transitions in perovskites, from a cubic parent structure to tetragonal and orthorhombic structures with space groups related to the M_3 and R_{25} points of the $Pm\bar{3}m$ reciprocal lattice. The equation permits relationships between symmetry-adapted forms of the spontaneous strain and individual order parameter components to be predicted. The symmetry-adapted strains, e_a (volume strain), e_o (orthorhombic strain) and e_t (tetragonal strain) are combinations of the linear strain components and are described as

$$e_a = (e_1 + e_2 + e_3),$$
$$e_o = (e_1 - e_2),$$
$$e_{tz} = (1/\sqrt{3})(2e_3 - e_1 - e_2).$$

The additional subscript, z, has been added to e_t in order to emphasize that the tetragonal axis is parallel to the reference Z-axis in this case (see Fig. 1 in Carpenter *et al.* (13)).

For the $I4/mcm$ structure, all the order parameter components are zero except q_4 and the spontaneous strain components are given by

$$e_1 = e_2 = \frac{a/\sqrt{2} - a_o}{a_o},$$

$$e_3 = \frac{c/2 - a_o}{a_o},$$

where a_o is the reference parameter of the cubic structure extrapolated into the tetragonal stability field, and a and c are the lattice parameters of the tetragonal structure. Under equilibrium conditions, $e_o = e_4 = 0$, and e_a and e_{tz} are proportional to the square of the order parameter q_4.

For the $Pnma$ structure, $q_1 = q_3 = q_5 = 0$ and $q_2 \neq 0$, $q_4 = q_6 \neq 0$. The individual strain components are given by

$$e_1 = \frac{b/2 - a_o}{a_o},$$

$$e_2 + e_3 = \frac{a/\sqrt{2} - a_o}{a_o} + \frac{c/\sqrt{2} - a_o}{a_o},$$

$$|e_4| = \left| \frac{a/\sqrt{2} - a_o}{a_o} - \frac{c/\sqrt{2} - a_o}{a_o} \right|,$$

where a, b and c are lattice parameters of the $Pnma$ structure. There is a tetragonal shear, which has its tetragonal axis parallel to the reference X-axis. This may be described as

$$e_{tx} = \frac{1}{\sqrt{3}}(2e_1 - e_2 - e_3).$$

Under equilibrium conditions $e_o = 0$, e_4 is proportional to the square of the order parameter component q_4 while e_a and e_{tx} scale with both q_2^2 and q_4^2.

3.2.2. Calculation of the Symmetry-Adapted Strains

The straight line a_0 shown in Fig. 3b is given by $3.82237 + 0.00005775T$ (in Å for temperature in °C), and was obtained by fitting the data points for the $Pm\bar{3}m$ structure between 940°C and 1000°C of the $x = 0.20$ sample. Due to the lack of data points for the sample with $x = 0.10$ in the cubic field, the straight line a_0 shown in Fig. 3a was built using the same slope as for the $x = 0.20$ sample and constraining the line to pass through the first cubic data point obtained by linear extrapolation of the tetragonal lattice parameters.

The spontaneous strains e_1, e_2, e_3 and e_4 were calculated according to the equations given for each structure in the preceding section. These were then used to calculate values for the symmetry-adapted strains e_{tx}, e_{tz} and e_a, which are shown together with e_4 in Figs. 9a and 9b for the $CaFe_{0.10}Ti_{0.90}O_{2.95}$ and $CaFe_{0.20}Ti_{0.80}O_{2.90}$ perovskites, respectively. The values of both e_4 and e_{tx} are relatively insensitive to the choice of the baseline, a_0, while
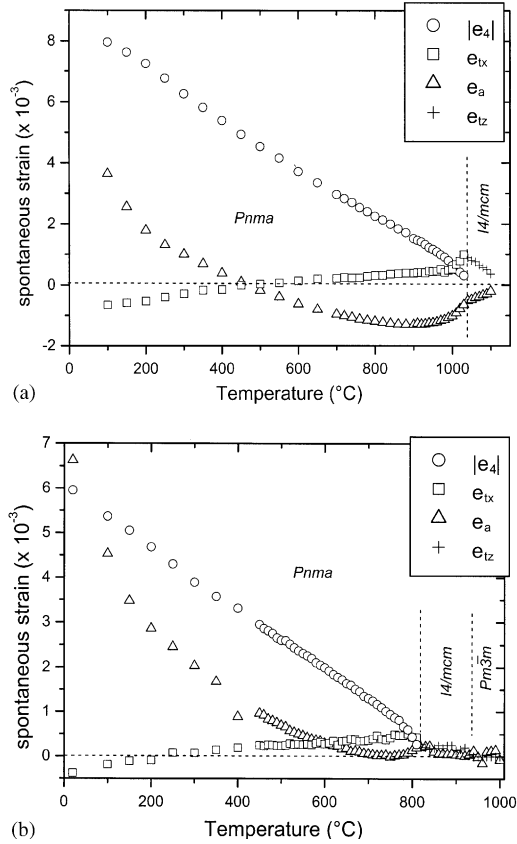
FIG. 9. Spontaneous strains for $CaFe_{0.10}Ti_{0.90}O_{2.95}$ (a) and $CaFe_{0.20}Ti_{0.80}O_{2.90}$ (b) as a function of temperature calculated from the lattice parameter data shown in Figs. 3a and 3b, respectively.

the volume strain values e_a are very sensitive to the choice of a_0.

3.2.3. Orthorhombic and Tetragonal Strains

The pattern of strain behavior in the orthorhombic field is very similar in both samples and agrees with the data reported by Carpenter et al. [13] for the pure $CaTiO_3$ perovskite. The absolute value of the individual strain component e_4 increases approximately linearly with falling temperature, developing discontinuosly from the tetragonal structure. This fact is consistent with the transition from tetragonal ($I4/mcm$) to orthorhombic ($Pnma$) being of first order in character, as expected from symmetry considerations [20]. The tetragonal shear e_{tx} is very small and changes sign in the vicinity of $425°C$ in the $x = 0.10$ sample and at around $250°C$ in the $x = 0.20$ sample. In the case of $CaTiO_3$, e_{tx} is also small and changes sign at $675°C$. The volume strain, e_a, is distinctly non-linear in the orthorhombic field for both compositions.

In the tetragonal field of the $CaFe_{0.10}Ti_{0.90}O_{2.95}$ sample (Fig. 9a), the tetragonal shear strain e_{tz} increases with decreasing temperature, reaching a maximum value of 0.009 in comparison with a maximum of ~ 0.005 for $CaTiO_3$. In the $CaFe_{0.20}Ti_{0.80}O_{2.90}$ perovskite, however, e_{tz} is very small (maximum of 0.0025) and shows a large scatter (Fig. 9b). Fig. 10a shows the variation of e_{tz}^2 with temperature in the $x = 0.10$ sample. In the absence of data points between $1100°C$ and the transition to cubic symmetry ($1120 \pm 25°C$), this variation seems to be linear. The cubic → tetragonal transition would, therefore, be close to tricritical in character, as is the case in the pure $CaTiO_3$ [12b, 13]. The linear fit in Fig. 10a gives a transition temperature of $\cong 1110°C$, which falls into the temperature range predicted for the transition. With such small strains,
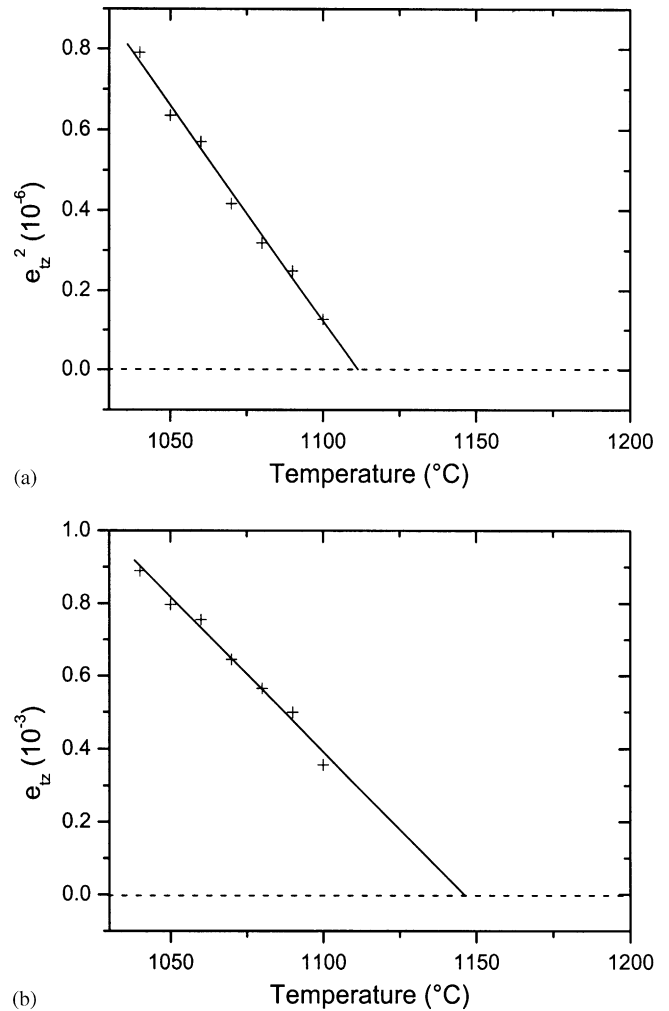

FIG. 10. (a) Square of the tetragonal strain vs temperature for the $I4/mcm$ structure of $CaFe_{0.10}Ti_{0.90}O_{2.95}$. The linear fit gives a transition temperature of $1110°C$ and would be consistent with tricritical character for the $Pm\bar{3}m \rightarrow I4/mcm$ transition. (b) Linear fit of the tetragonal strain for the same phase giving a transition temperature of $1145°C$ for second-order character. More data points close to the transition are necessary to distinguish between the two possibilities.

the plot of e_{tz} vs. temperature (Fig. 10b) can also be fitted to a straight line, however, giving $T_c \cong 1145°C$ for second-order character. More data close to the transition point are therefore needed to determine the thermodynamic character definitively.

3.2.4. Strain-Strain and Strain-Order Parameter Relationships

The relationships between symmetry-adapted strains and order parameter components, given by Carpenter et al. (13) and briefly explained in Section 3.2.1 above, can be tested for self-consistency by plotting one strain against another. Plots of strain/strain variations are shown in Fig. 11 for the $x = 0.10$ and 0.20 samples. Both e_{tz} and e_a for the $I4/mcm$ structure are expected to scale with q_4^2 and they do indeed vary linearly with respect to each other in the $x = 0.10$ sample, as shown in Fig. 11a. The plot of e_{tz} vs e_a shows very low and roughly constant values for the $x = 0.20$ sample, however. In the $Pnma$ structure a non-linear behavior is observed for e_{tx} as a function of e_a in both samples (Fig. 11a). A non-linear behavior is also shown by the $CaTiO_3$ end-member (13). In the $Pnma$ structure, the shear strain e_4 has two segments (Fig. 11b), increasing non-linearly with decreasing e_a but then reversing in slope. A similar behavior is observed in $CaTiO_3$, where the segments could be linear, as opposed to the definite non-linearity shown in the Fe-containing samples. Finally, Fig. 11c shows the behavior of e_{tx} vs e_4, where a more or less linear trend is observed. These results suggest that the anomalous evolution of $Pnma$ strains is associated largely with e_a.

In order to test whether the non-linearities evident in Figs. 9 and 11 signify higher-order coupling effects or variations of two-order parameter components with respect to each other in the $Pnma$ structure, it is necessary to have some independent measure of how each of q_2 and q_4 evolve. A way of measuring the order parameter variation is through the general relationship $Q^2 \propto I_k$, where Q is the order parameter for a transition and I_k is the intensity of a superlattice reflection, which appears as a consequence of the transition. We have measured the intensities of 031 and 102 reflections (I_{031}, I_{102}), which have zero intensity under $Pm\bar{3}m$ symmetry and arise at the $Pm\bar{3}m \leftrightarrow I4/mcm$ and $I4/mcm \leftrightarrow Pnma$ transitions, respectively. It is assumed that I_{031} is proportional to q_4^2 and I_{102} is proportional to q_2^2. Both I_{031} and I_{102} decrease with increasing temperature for both Fe-doped $CaTiO_3$ perovskites, as shown in Figs. 12a and 13a. A plot of I_{102} vs I_{031} (Figs. 12b and 13b) is then effectively a plot of q_2^2 vs q_4^2. The lines drawn through the data are guides to the eye for an interpretation in which $q_2 = 0$ and $q_4 \neq 0$ in the $I4/mcm$ phase followed by a first order transition (dashed line) to the $Pnma$ structure with $q_2 \neq 0$ and $q_4 \neq 0$. Note that these lines would extrapolate to the origin for the case of $T_{c1} =$
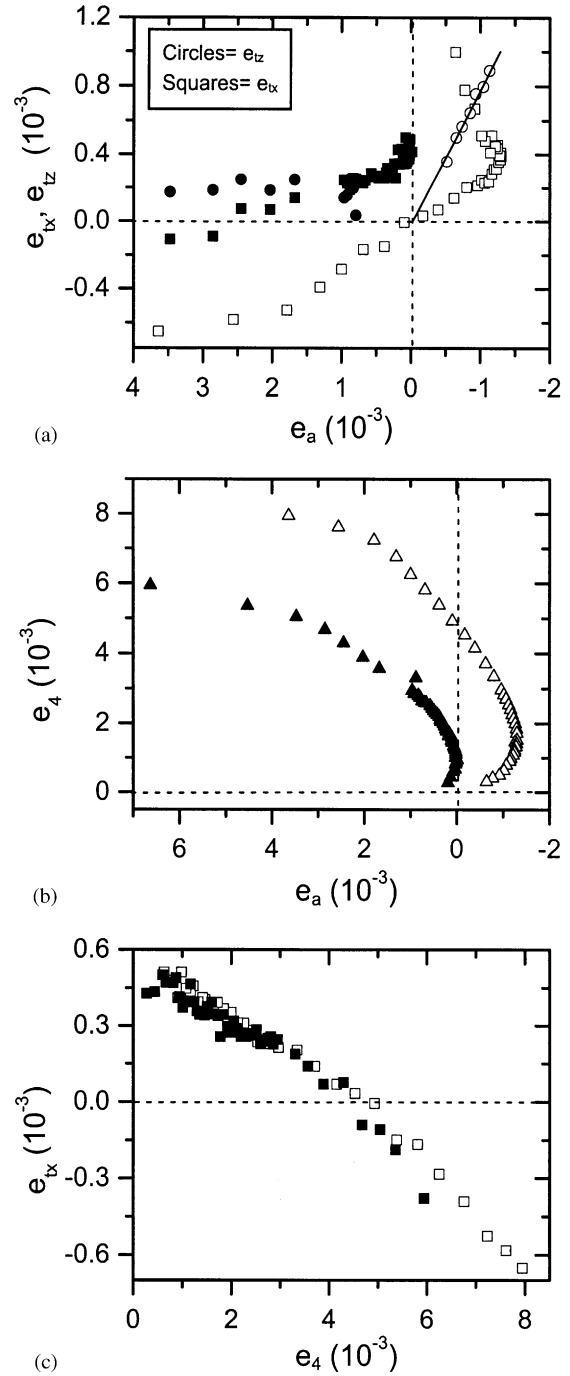

FIG. 11. Strain–strain relationships for the $I4/mcm$ and $Pnma$ structures as a function of temperature in the $CaFe_{0.10}Ti_{0.90}O_{2.95}$ (open symbols) and $CaFe_{0.20}Ti_{0.80}O_{2.90}$ (solid symbols) perovskites. The linear relationship between e_{tz} and e_a and between e_{tx} and e_4 are clear, while e_a behaves in a distinctly non-linear manner with respect to both e_4 and the tetragonal strain e_{tx}. Values of e_{tz} in the $x = 0.20$ sample (solid circles) are very small and roughly constant with e_a.

T_{c2}, where T_{c1} and T_{c2} are critical temperatures associated with the M and R points. With increasing $CaFeO_{2.5}$ content the linear fit more nearly extrapolates through the
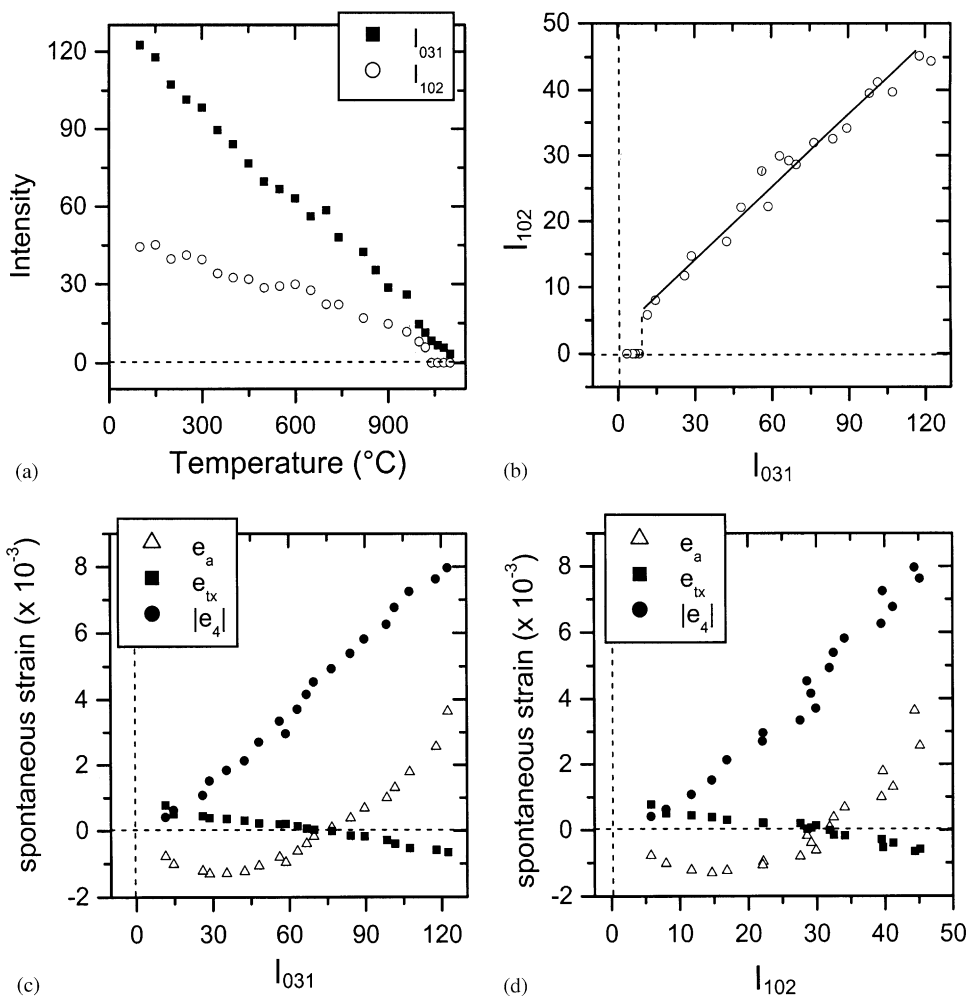
FIG. 12. Relationships between superlattice reflection intensities and *Pnma* spontaneous strains for $CaFe_{0.10}Ti_{0.90}O_{2.95}$. The intensities I_{031} and I_{102} are expected to be proportional to q_2^2 and q_4^2, respectively. (a) Variation of q_2^2 and q_4^2 with temperature. (b) Variation of I_{102} with I_{031}. (c and d) The shear strain e_4 is, within experimental error, proportional to I_{031} and to I_{102} and, therefore, it is also proportional to q_4^2 and q_2^2, as expected. The tetragonal shear, e_{tx}, is linear with both while the volume strain, e_a, is markedly non-linear with I_{031} and I_{102}.

origin, implying that the critical temperatures T_{c1} and T_{c2} converge across the solid solution.

Both I_{031} and e_4 are expected to scale linearly with q_4^2 and, within experimental error, they appear to do so (Figs. 12c and 13c). The remaining strains depend on both q_2^2 and q_4^2 and, while e_{tx} and e_4 vary approximately linearly with I_{102}, it is clear that e_a is markedly non-linear with respect to both I_{102} and I_{031} (Figs. 12c and 12d and Figs. 13c and 13d). We can therefore infer that e_4, e_{tx}, q_2^2 and q_4^2 behave more or less classically, as described by order parameter coupling and shear strain/order parameter coupling models. However, the volume strain, e_a, has an anomalous coupling with either q_2^2 or q_4^2 (or both) and, therefore, the coupling coefficients λ_1 and λ_2 in the Landau free energy expansion which describes these phase transitions (Eq. [1] in (13)) may have a temperature dependence, as found for pure CaTiO₃.

The non-linear coupling behavior of the volume strain with respect to the square of the order parameter has also been described for the pure CaTiO₃ perovskite (13) as well as for other perovskite-type compounds (21). This behaviour can be due to temperature-dependent coupling coefficients or higher-order coupling effects. The first cause would certainly change the pattern of evolution of the order parameter as a function of temperature. Considering the tetragonal↔orthorhombic transition in Fe-doped CaTiO₃ perovskites, the shear strain e_4 scales with temperature as $e_4 \propto |T - T_c|$ for $T \ll T_c$ but as $e_4^2 \propto |T - T_c|$ when T is close to T_c (Figs. 9a and 9b). This change is consistent with a temperature dependence for the coefficients which are fourth order in q if at high temperatures the coefficient is large but then becomes smaller as temperature is reduced. A strong coupling with e_a at high temperatures reducing to much weaker coupling at low
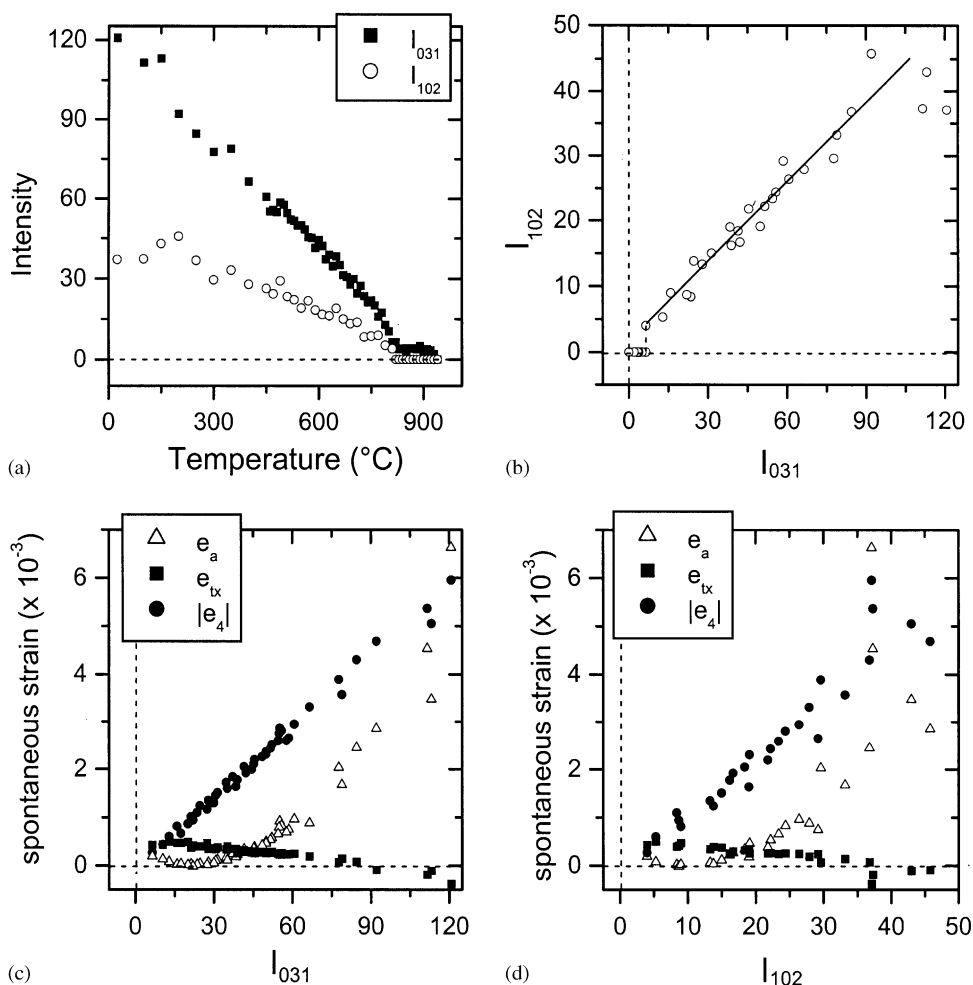
FIG. 13. Relationships between superlattice reflection intensities and *Pnma* spontaneous strains for $CaFe_{0.20}Ti_{0.80}O_{2.90}$. The intensities I_{031} and I_{102} are expected to be proportional to q_2^2 and q_4^2, respectively. (a) Variation of q_2^2 and q_4^2 with temperature. (b) Variation of I_{102} with I_{031}. (c and d) The shear strain e_4 is, within experimental error, proportional to I_{031} and to I_{102} and, therefore, it is also proportional to q_4^2 and q_2^2, as expected. The tetragonal shear, e_{tx}, is linear with both while the volume strain, e_a, is markedly non-linear with I_{031} and I_{102}.

temperatures could have exactly this effect. This type of coupling is observed in $NaMgF_3$ for the cubic ↔ orthorhombic transition (13).

REFERENCES

1. P. M. Woodward, *Acta Crystallogr. B* **53,** 44 (1997).
2. (a) B. J. Wood and D. C. Rubie, *Science* **273,** 1522 (1996); (b) C. McCammon, *Nature* **387,** 694 (1997).
3. (a) J. C. Grenier, M. Darriet, M. Pouchard, and P. Hagenmuller, *Mater. Res. Bull.* **11,** 1219 1976; (b) J. C. Grenier, G. Schiffmacher, P. Caro, M. Pouchard, and P. Hagenmuller, *J. Solid State Chem.* **20,** 365 (1977); (c) J. C. Grenier, M. Pouchard, and P. Hagenmuller, *Mater. Res. Bull.* **13,** 329 (1978).
4. A. A. Colville, *Acta Crystallogr. B* **26,** 1469 (1970).
5. J. Rodríguez-Carvajal, M. Vallet-Regí, and J. M. González Calbet, *Mater. Res. Bull.* **24,** 423 (1989).
6. S. Hovmöller, X. Zou, D. Neng Wang, J. M. González-Calbet, and M. Vallet-Regí, *J. Solid State Chem.* **77,** 316 (1988).
7. A. I. Becerro, C. McCammon, F. Langenhorst, R.J. Angel, and F. Seifert, *Phase Transitions* **69,** 133 (1999).
8. A. I. Becerro, F. Seifert, R. J. Angel, S. Ríos, and C. McCammon, *J. Phys.: Condens. Matter.* **12,** 3661 (2000).
9. (a) C. McCammon, A. I. Becerro, F. Langenhorst, R. J. Angel, S. Marion, and F. Seifert, *J. Phys.: Condens. Matter.* **12,** 2969 (2000); (b) A. I. Becerro, M. A. Carpenter, T. Boffa-Ballaran, and F. Seifert, *Phase Transitions* **71,** 161 (2000); (c) A. I. Becerro, F. Langenhorst, R. J. Angel, S. Marion, C. McCammon, and F. Seifert, *Phys. Chem. Chem. Phys.* **2,** 3933 (2000).
10. S. Sasaki, *Acta Crystallogr. C* **43,** 1668 (1987).
11. S. A. T. Redfern, *J. Phys.: Condens. Matter* **8,** 8267 (1996).

12. (a) F. Guyot, P. Richet, Ph. Courtial, and Ph. Gillet, *Phys. Chem. Miner*. **20,** 141 (1993); (b) B. J. Kennedy, C. J. Howard, and B. C. Chakoumakos, *J. Phys.: Condens. Matter* **11,** 1479 (1999).

13. M. A. Carpenter, A. I. Becerro, and F. Seifert, *Amer. Mineral*. **86,** 348 (2001).

14. R. M. Ibberson, W. I. F. David, and K. S. Knight, "The High-Resolution Powder Diffractometer (HRPD) at ISIS—a User Guide," Report RAL-92-031. Rutherford Appleton Laboratory, Chilton, Didcot, England, 1992.

15. A. C. Larson and R.B. Von Dreele, "GSAS: General Structural Analysis System," LANSCE, Los Alamos National Laboratory, Los Alamos, NM, The Regents of the University of California, 1994.

16. A. M. Glazer, *Acta Crystallogr. B* **28,** 3384 (1972).

17. X. Liu, Y. Wang, R. C. Liebermann, P. D. Maniar, and A. Navrotsky, *Phys. Chem. Minerals* **18,** 224 (1991).

18. (a) C. J. Howard, R. L. Withers, and B. J. Kennedy, *J. Solid State Chem*. **160,** 8 (2001); (b) R. Ranjan, D. Pandey, W. Schuddinck, O. Richard, P. De Meulenaere, J. Van Landuyt, and G. Van Tendeloo, *J. Solid State Chem*. **162,** 20 (2001).

19. J. N. Street, unpublished Ph.D. Thesis, University College, London.

20. C. J. Howard and H. T. Stokes, *Acta Crystallogr. B* **54,** 782 (1998).

21. (a) Y. Zhao, D. J. Weidner, J. B. Parise, and D. E. Cox, *Phys. Earth Planet. Int*. **76,** 1 (1993); (b) M. A. Carpenter, E. K. H. Salje, and A. Graeme-Barber, *Eur. J. Miner*. **10,** 621 (1998); (c) K. S. Knight, *Solid State Ionics* **74,** 109 (1994); (d) M. A. Carpenter, E. K. H. Salje, A. Graeme-Barber, B. Wruck, M. T. Dove, and K. S. Knight, *Amer. Miner*. **83,** 2 (1998); (e) C. N. W. Darlington, *Phys. Status Sol. A* **155,** 31 (1996); (f) A. Gibaud, S. M. Shapiro, J. Nouet, and H. You, *Phys. Rev. B* **44,** 2437 (1991); (g) M. A. Carpenter and E. K. H. Salje, *Eur. J. Miner*. **10,** 396 (1998).